

RSC Advances

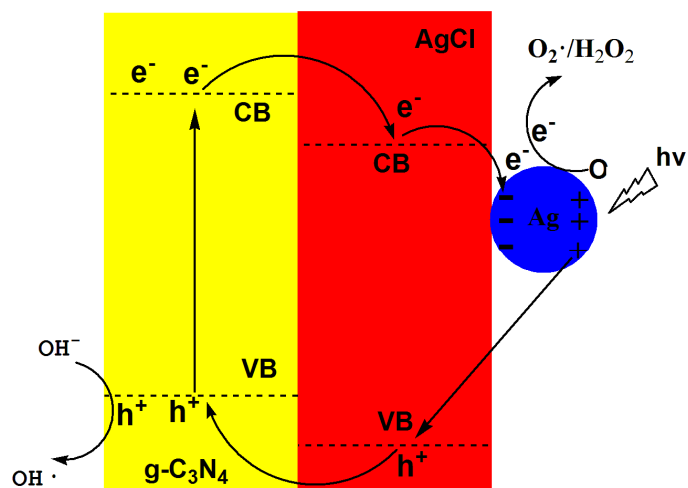


This is an *Accepted Manuscript*, which has been through the Royal Society of Chemistry peer review process and has been accepted for publication.

Accepted Manuscripts are published online shortly after acceptance, before technical editing, formatting and proof reading. Using this free service, authors can make their results available to the community, in citable form, before we publish the edited article. This *Accepted Manuscript* will be replaced by the edited, formatted and paginated article as soon as this is available.

You can find more information about *Accepted Manuscripts* in the [Information for Authors](#).

Please note that technical editing may introduce minor changes to the text and/or graphics, which may alter content. The journal's standard [Terms & Conditions](#) and the [Ethical guidelines](#) still apply. In no event shall the Royal Society of Chemistry be held responsible for any errors or omissions in this *Accepted Manuscript* or any consequences arising from the use of any information it contains.



The formation of an effective heterojunction electric field at the interface between g-C₃N₄ and Ag@AgCl significantly strengthens the separation efficiency of the photogenerated electrons and holes, leading to a dramatic promotion of the photocatalytic degradation performance.

ARTICLE

Study of the Promotion Mechanism of the Photocatalytic Performance and Stability of the Ag@AgCl/g-C₃N₄ Composite under Visible Light

Cite this: DOI: 10.1039/x0xx00000x

Yuyu Bu^a, Zhuoyuan Chen^{*a}, Chang Feng^b and Weibing Li^b

Received 00th January 2012,
Accepted 00th January 2012

DOI: 10.1039/x0xx00000x

www.rsc.org/

The Ag@AgCl/g-C₃N₄ composite was prepared by in situ fabricating Ag@AgCl on the surface of g-C₃N₄ using deposition-precipitation and subsequently photo-assisted reduction. Both the photocatalytic degradation performance and the photocatalytic degradation stability of the Ag@AgCl/g-C₃N₄ composite are significantly improved compared with that of g-C₃N₄ and Ag@AgCl composite. The Ag@AgCl/g-C₃N₄ composite can completely degrade RhB in 20 min under the illumination of visible light ($\lambda > 420$ nm). The Ag@AgCl/g-C₃N₄ composite can increase the light absorption intensity in visible light region due to the surface plasmon resonance effect of Ag, resulting in a significant increase of the yields of the photogenerated electrons and holes. An effective heterojunction electric field was formed on the interface between g-C₃N₄ and Ag@AgCl, which significantly strengthened the separation efficiency of the photogenerated electrons and holes, leading to a significant promotion of the photocatalytic degradation performance.

Introduction

Photocatalytic technology is one of the key technologies to solve the issues of energy shortage and environmental pollution. So far, this technology has experienced more than 40 years of development and has made considerable progress. However, the narrow photoresponse range and the low photo quantum yield of the photocatalysts are the two key factors which restrict their practical application. Related studies¹⁻⁴ indicated that the methods to extend the light absorption range of photocatalysts mainly include: (1) preparing novel photocatalysts with visible light absorption capability;⁵⁻⁸ (2) doping with metallic or nonmetallic elements;⁹⁻¹¹ (3) sensitizing or compositing with narrow bandgap semiconductor.^{12,13} The methods to improve the photo quantum yield of photocatalysts mainly include: (1) constructing heterojunction system by compositing with other

semiconductor materials to improve the separation efficiency of photogenerated electrons and holes through the heterojunction electric field;¹⁴⁻¹⁶ (2) increasing the specific surface areas of semiconductor materials to increase the reactive sites of photocatalytic reactions;¹⁷⁻¹⁸ (3) fabricating special topographies of semiconductor materials to promote the migration efficiency of the photogenerated electrons and therefore to effectively restrain the secondary recombination of the photogenerated electrons and holes.¹⁹⁻²²

In recent years, g-C₃N₄, acted as a photocatalyst, has attracted widespread concern. In 2009, Wang et al.⁵, for the first time, reported that g-C₃N₄ can generate hydrogen by splitting water under visible light and the bandgap of g-C₃N₄ is 2.7 eV. Subsequently, Yan et al.²³ reported that g-C₃N₄ can degrade organic pollutants under visible light. And,

Zhang et al²⁴ confirmed that g-C₃N₄ has the characteristics of n-type semiconductor using Mott-Schottky method. The conduction band potential of g-C₃N₄ is -1.42 V (vs Ag/AgCl) and its valence band potential is 1.25 V (vs Ag/AgCl). However, further studies found that the less photocatalytic reaction active sites, the lower separation efficiency and migration rates of the photogenerated electrons, and the more negative valence band potential restrict the further promotion of the photocatalytic performance of g-C₃N₄. In order to solve the above issues, mesoporous g-C₃N₄ was prepared using hard template method¹⁷ and soft template method²⁵. Investigations showed that the number of the active photocatalytic reaction sites of mesoporous g-C₃N₄ was significantly enhanced, resulting in the dramatic increase of its photocatalytic performance. Recently, Zhang et al²⁶ reported that two-dimensional ultrathin C₃N₄ nanosheet (2D-C₃N₄) can be fabricated by ultrasonically dispersing g-C₃N₄. The specific surface area and electron mobility of this 2D-C₃N₄ are greatly improved comparing with those of g-C₃N₄, resulting in a significant increase of the photocatalytic performance of 2D-C₃N₄. Zhang et al²⁷ reported that the conductivity of g-C₃N₄ was greatly improved by doping with proton acid. Zhang et al²⁸ found that doping g-C₃N₄ with P can significantly enhance its conductivity through simulated calculation. Zhang et al²⁹ prepared S-doped g-C₃N₄ and they found that the introducing of S can positively shift the valence band potential of g-C₃N₄, thereby enhancing the oxidation capability of the photogenerated holes. Subsequently, Ma et al³⁰ reported that doping S into g-C₃N₄ can move the valence band to a more positive potential according to the first-principles density functional theory. To further enhance the separation efficiency of the photogenerated electrons and holes, g-C₃N₄ was

composited with noble metal or other semiconductor materials to build a heterojunction system.³¹⁻³⁷ The heterojunction electric field formed on the interface between them restrained the secondary recombination of the photogenerated electrons and holes, thus effectively enhancing the photocatalytic performance of g-C₃N₄.

The Ag@AgX (Cl, Br, I) composites with surface plasmon resonance (SPR) effect have been gradually becoming the focus of research in the field of photocatalysis in recent years. These materials can absorb light nearly over the entire visible light region, and they can convert photons into separated photogenerated electrons and holes through the collective oscillations of the surface electrons.³⁸⁻⁴¹ However, the photoinduced electrons and holes generated by these composites are prone to secondary recombination, resulting in the decrease of photocatalytic performance. Furthermore, the high price of Ag@AgX restricts its practical application. Compositing Ag@AgX with other materials, such as TiO₂,⁴² ZnO,⁴³ Ag₃PO₄,⁴⁴ Bi₂WO₃,⁴⁵ and graphene⁴⁶ etc., could build a heterojunction electric field. With the aid of this heterojunction electric field, the photoinduced electrons and holes generated by Ag@AgX could be effectively separated, leading to a significant increase of the photocatalytic performance of Ag@AgX.^{47,48} Meanwhile, the introducing of these low-cost semiconductor materials could decrease the usage of Ag@AgX, which can reduce the cost and enhance the practical application potential of such photocatalyst.

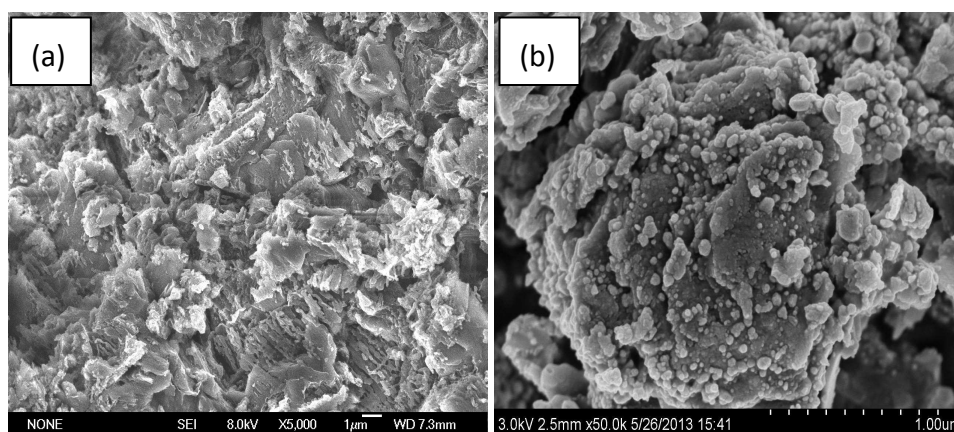
Based on the above descriptions, the photocatalytic performance of the Ag@AgCl/g-C₃N₄ composite was expected to be very good; therefore, it is necessary to study the photocatalytic properties of this composite. In this paper, the authors prepared the Ag@AgCl/g-

C_3N_4 composite and investigated the photocatalytic degradation performance and photocatalytic stability of this composite. And, the promotion mechanism of the photocatalytic performance of the $Ag@AgCl/g-C_3N_4$ composite was also studied using electrochemical /photoelectrochemical test methods.

Results and discussion

Figure 1 shows the SEM images of the prepared $g-C_3N_4$, $Ag/g-C_3N_4$, $AgCl/g-C_3N_4$ and $Ag@AgCl/g-C_3N_4$, and the TEM morphologies of the prepared $Ag@AgCl/g-C_3N_4$ composite. Figure 1a shows the SEM image of the prepared $g-C_3N_4$, and a layered stacking structure is clearly identified, which has the basic characteristics of the substance of a graphite-like structure. Figure 1b shows the SEM image of the prepared $Ag/g-C_3N_4$ composite, which shows that Ag nanoparticles are successfully modified onto $g-C_3N_4$ by photo-assisted reduction. And, a large number of Ag nanoparticles distributed on the surface of the $g-C_3N_4$ are of approximately 10~50 nm in diameter. Figure 1c shows the SEM image of the prepared

$AgCl/g-C_3N_4$ composite, and a lot of lumps are observed on the surface of $g-C_3N_4$, which could be AgCl. Figure 1d shows the SEM image of the prepared $Ag@AgCl/g-C_3N_4$ composite. As shown in Figure 1d, a lot of nanoparticles with diameter of approximately 50 nm were formed on the surface of the lumps as observed in Figure 1c. These nanoparticles could be Ag particles reduced from AgCl deposited on the surface of $g-C_3N_4$ by photo-assisted reduction. TEM was used to further characterize the distribution of $Ag@AgCl$ on the surface of $g-C_3N_4$ and the results are shown in Figures 1e and 1f. Figure 1e shows the microscopic morphology under low magnification. As shown in Figure 1e, a large number of $Ag@AgCl$ nanoparticles distribute uniformly and densely on the surface of $g-C_3N_4$. Under high magnification (Figure 1f), the nanoparticles with diameter of approximately 50 nm can be clearly observed.



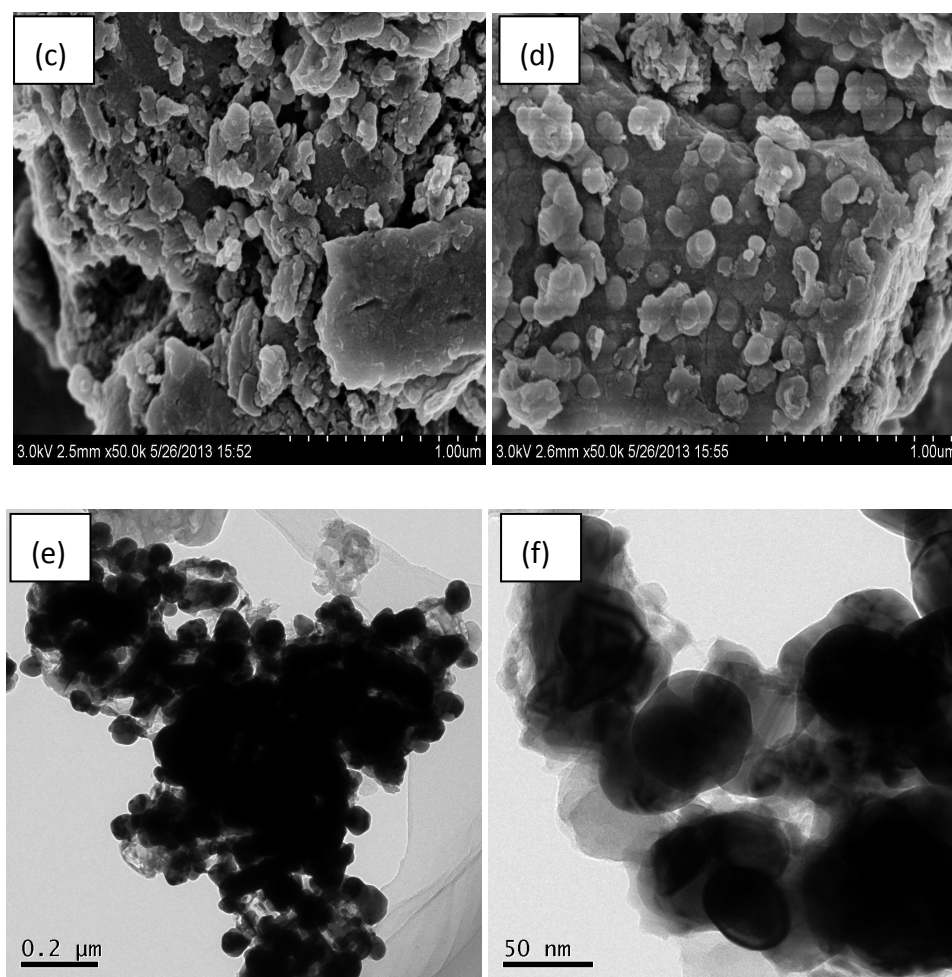


Figure 1. SEM of (a) $g\text{-C}_3\text{N}_4$; (b) $\text{Ag}/g\text{-C}_3\text{N}_4$; (c) $\text{AgCl}/g\text{-C}_3\text{N}_4$; (d) $\text{Ag@AgCl}/g\text{-C}_3\text{N}_4$; TEM of $\text{Ag@AgCl}/g\text{-C}_3\text{N}_4$ at low (e) and high (f) resolution.

Figure 2 shows the XRD patterns of the series of the prepared samples. Curve 2a is the XRD pattern of the $g\text{-C}_3\text{N}_4$ powder prepared in the present work. A high-intensity diffraction peak is observed in $2\theta = 27.4^\circ$, which is the characteristic index of the interlayer stacking of aromatic series. The calculated interplanar distance of the aromatic series is $d = 0.324$ nm. This observation shows that the material has a layered structure, similar to that of graphite. Curve 2b is the XRD pattern of the Ag@AgCl powder prepared in the present work. The diffraction peaks at $2\theta = 27.82^\circ$,

32.24° , 46.25° , 54.81° , and 57.56° , marked with “□” in Figure 2, are assigned to the (111), (200), (220), (311), and (222) crystal planes of AgCl (JCPDS cards nos. 31-1238). The characteristic diffraction peaks of Ag at $2\theta = 38.1^\circ$ and 44.3° , which are assigned to (111) and (200) crystal planes of Ag (JCPDS cards nos. 04-0783), are not observed. This could be caused by the low yield or low crystallinity of Ag formed on AgCl . Curve 2c is the XRD pattern of the prepared $\text{Ag}/g\text{-C}_3\text{N}_4$ powder. Except for a weak peak at $2\theta = 27.4^\circ$, the characteristic diffraction peaks of Ag

observed at $2\theta = 38.1^\circ$ and 44.3° are marked with “o” in Figure 2. Curve 2d is XRD pattern of AgCl/g- C_3N_4 , from which the characteristic diffraction peaks of AgCl were observed at 27.82° , 32.24° , 46.25° , 54.81° , and 57.56° , which are the same as those observed in Curve 2b. Curve 2e is the XRD pattern of Ag@AgCl/g- C_3N_4 . Except for the diffraction peaks from AgCl, two very weak diffraction peaks from Ag were observed at $2\theta = 38.1^\circ$ and 44.3° , which demonstrates that Ag is grown on the surface of AgCl.

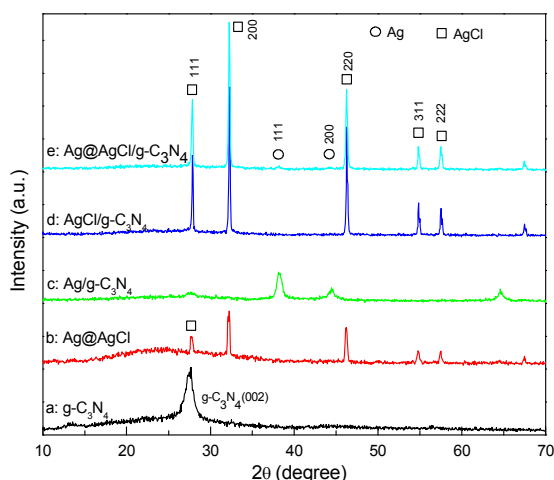


Figure 2. XRD patterns of (a) g- C_3N_4 ; (b) Ag@AgCl; (c) Ag/g- C_3N_4 ; (d) AgCl/g- C_3N_4 ; (e) Ag@AgCl/g- C_3N_4 .

Figure 3 shows the XPS spectra of the Ag@AgCl/g- C_3N_4 composite. Figures 3a, 3b, 3c and 3d show the C1s, N1s, Ag3d and Cl2p XPS core level spectra, respectively. Binding energy peaks at 284.6 and 288.1 eV in Figure 3a can be ascribed to carbon and defect-containing sp^2 -bonded carbon (C=N). Binding energy peak at 398.8 eV in Figure 3b can be ascribed to the sp^2 -hybridized C=N-C.^{31,49} Binding energy peaks at 367.6 and 373.6 eV in Figure 3c are assigned to the

electron orbits of Ag 3d $_{5/2}$ and Ag 3d $_{3/2}$, which is attributed to Ag⁺ from AgCl.⁵⁰ Binding energy peaks at 198.1 and 199.6 eV in Figure 3d represent the characteristic ones of Cl 2p $_{5/2}$ and Cl 2p $_{3/2}$, respectively, which demonstrates that Cl is existed as Cl⁻. The results obtained in this work are in good agreement with those from literature.^{31,47,50}

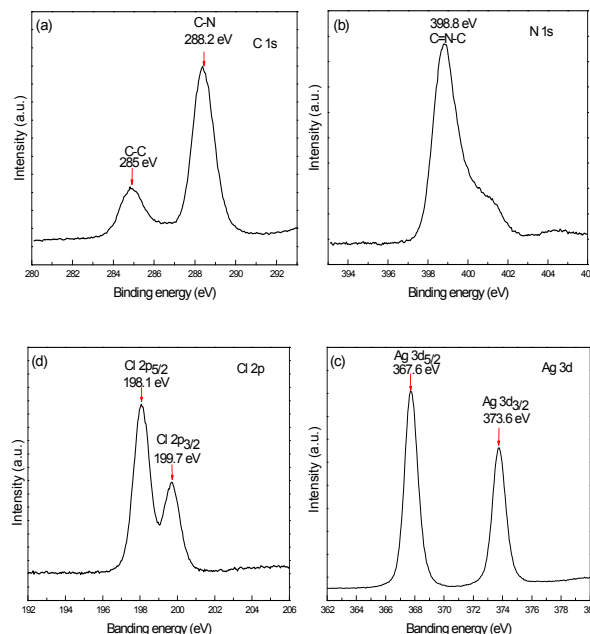


Figure 3. XPS spectra of Ag@AgCl/g- C_3N_4 (a) C 1s; (b) N 1s; (c) Ag 3d; (d) Cl 2p.

Figure 4 shows the UV/Vis diffuse reflectance spectra of the series of the prepared samples. The absorption bandedge of g- C_3N_4 is approximately 460 nm (Curve 4a), which is in agreement with that from Wang et al.⁵ The absorption of the Ag/g- C_3N_4 composite is very strong in the whole wavelength range, as shown in Curve 4b. This can be caused by the adsorption of Ag on this composite. The Ag nanoparticles distributed on the surface of g- C_3N_4 will

darken the Ag/g-C₃N₄ composite, leading to a strong absorption of the incident light. However, this absorption cannot change to the energy for generating the electron-hole pairs and it is just converted to heat dissipation. The absorption bandedge of the AgCl/g-C₃N₄ composite is approximately 450 nm (Curve 4c). The slight blue shift of the absorption bandedge of the AgCl/g-C₃N₄ composite is attributed to the introducing of AgCl into the composite. AgCl is a semiconductor with a large bandgap, whose bandedge is approximately 380 nm. The absorption intensity of the AgCl/g-C₃N₄ composite is slightly higher than that of g-C₃N₄ in the wavelength of <450 nm. Curve 4d shows the UV/Vis diffuse reflectance spectrum of the Ag@AgCl/g-C₃N₄ composite, from which it represents the strongest absorption capacity in the wavelength range of 250-700 nm. Meanwhile, a broad absorption peak at around of 500 nm is observed, which is caused by the SPR effect of Ag@AgCl. The UV/Vis results of the Ag@AgCl/g-C₃N₄ composite indicate that this composite has very strong light absorption capability in the visible light region.

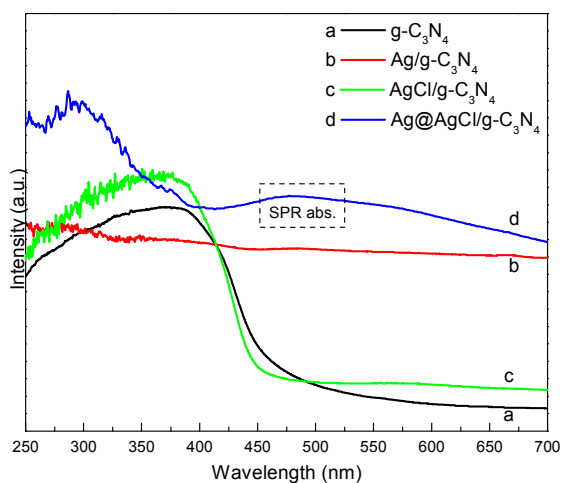


Figure 4. UV/Vis diffuse reflectance spectra of (a) g-C₃N₄; (b) Ag/g-C₃N₄; (c) AgCl/g-C₃N₄; (d) Ag@AgCl/g-C₃N₄.

Figure 5 shows the RhB degradation curves of the series of the prepared photocatalysts. Before the light was switched on, the photocatalysts were mixed with the RhB under dark conditions and stirred for 30 min. According to the data obtained for the 30 min adsorption under dark conditions, Ag/AgCl shows the lowest adsorption capacity, and Ag/g-C₃N₄ shows the highest adsorption capacity. The adsorption capacity of g-C₃N₄, AgCl/g-C₃N₄ and Ag@AgCl/g-C₃N₄ are similar, and all of them are located between Ag@AgCl and Ag/g-C₃N₄. And, g-C₃N₄ demonstrated a quite good capacity for the photocatalytic degradation of RhB. About 55.5% RhB was degraded by g-C₃N₄ after 50 min of illumination under visible light (Curve 5a). The photocatalytic degradation ability of Ag@AgCl is better than that of g-C₃N₄. And, 64.1% RhB can be degraded by Ag@AgCl in 50 min under visible light, as shown in Curve 5b. After loading Ag on the surface of g-C₃N₄, its adsorption capability was dramatically strengthened, as shown in Curve 5c; however, its photocatalytic degradation capability was significantly decreased. The excessive Ag on the surface of g-C₃N₄ can act as the recombination centers of the photogenerated electrons and holes, resulting in the decreasing of the photocatalytic degradation performance. For AgCl/g-C₃N₄ composite, 72% RhB was degraded by it after 50 min of illumination under visible light (Curve 5d), indicating that loading AgCl with g-C₃N₄ can

significantly increase the photocatalytic degradation performance of both $g\text{-C}_3\text{N}_4$ and AgCl. For the $\text{Ag@AgCl}/g\text{-C}_3\text{N}_4$ composite, all of RhB can be completely degraded after only 20 min of illumination by visible light, exhibiting a very strong photocatalytic degradation performance.

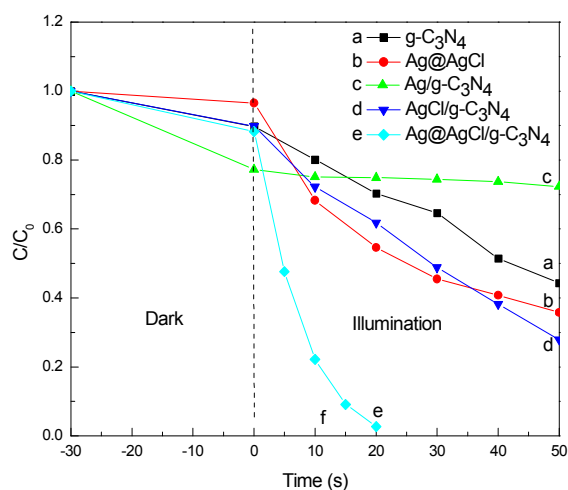


Figure 5. Visible light photocatalytic degradation RhB by (a) $g\text{-C}_3\text{N}_4$; (b) Ag@AgCl ; (c) $\text{Ag}/g\text{-C}_3\text{N}_4$; (d) $\text{AgCl}/g\text{-C}_3\text{N}_4$; and (e) $\text{Ag@AgCl}/g\text{-C}_3\text{N}_4$.

As shown in Figure 5, $\text{Ag}/g\text{-C}_3\text{N}_4$ possesses the strongest RhB adsorption capacity although it cannot degrade RhB dye. In order to obtain the causes of the phenomenon, the specific surface areas of $g\text{-C}_3\text{N}_4$, $\text{Ag}/g\text{-C}_3\text{N}_4$ and $\text{Ag@AgCl}/g\text{-C}_3\text{N}_4$ were measured using BET method and the relevant results are shown in Figure S1. As shown in Figure S1, the specific surface areas of $g\text{-C}_3\text{N}_4$, $\text{Ag}/g\text{-C}_3\text{N}_4$ and $\text{Ag@AgCl}/g\text{-C}_3\text{N}_4$ are 9.2425, 1.3123 and 14.4307 $\text{m}^2\cdot\text{g}^{-1}$, respectively. Apparently $\text{Ag}/g\text{-C}_3\text{N}_4$ has the minimum specific surface area. Based on the shapes of the Nitrogen adsorption-desorption curves in Figure S1, all of

these three materials can be classified as IV-type adsorption-desorption characteristic, demonstrating that these materials have the mesoporous structures, which are formed mainly by the stacking of C_3N_4 materials. As shown in Curve b of Figure S1, negative values were observed on the Y axis in the adsorption-desorption curve of $\text{Ag}/g\text{-C}_3\text{N}_4$, illustrating that there exist large amounts of non-porous structures in $\text{Ag}/g\text{-C}_3\text{N}_4$. A large amount of Ag particles is loaded on the surface of $g\text{-C}_3\text{N}_4$ which blocks most of the mesopores formed by the stacking of C_3N_4 materials, leading to the formation of a large amount of non-porous structures in $\text{Ag}/g\text{-C}_3\text{N}_4$ and thus decreasing the specific surface area of $\text{Ag}/g\text{-C}_3\text{N}_4$. Although it has the minimum specific surface area, $\text{Ag}/g\text{-C}_3\text{N}_4$ possesses the strongest adsorption capacity for RhB. As we may know, RhB is azo dyes in which the N atom in the molecular chain has outer lone pair electrons. While the unoccupied orbit of the outmost shell of Ag is easy to combine with the lone pair electrons of the N atoms of RhB dye, resulting in the dramatic increase of the adsorption capacity of this material.

In order to investigate the stability of the $\text{Ag@AgCl}/g\text{-C}_3\text{N}_4$ composite in the process of photocatalysis, six successive cyclic RhB degradation tests were performed and the relevant experimental results are shown in Figure 6. From the results shown in Figure 6, the photocatalytic RhB degradation efficiency of this composite material does not show noticeable decline after six successive cyclic RhB degradation tests and this composite can still degrade 90% RhB after 60 min of illumination by visible light

at the 6th degradation cycle, demonstrating that this composite possesses very high photocatalytic degradation stability.

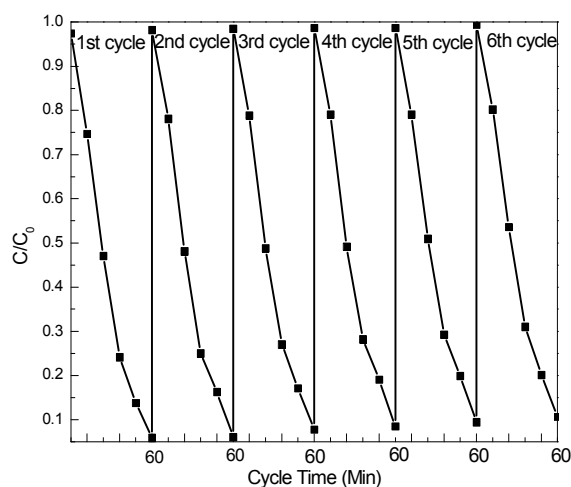


Figure 6. Stability study for the photocatalytic RhB degradation by the Ag@AgCl/g-C₃N₄ composite under visible light.

To further study the significant promotion mechanism of the photocatalytic degradation efficiency of the Ag@AgCl/g-C₃N₄ composite, the photoinduced current densities of the photoelectrodes prepared using g-C₃N₄ and the Ag@AgCl/g-C₃N₄ composite were measured at a 0 V (vs Ag/AgCl) bias potential under visible light and the results are shown in Figure 7. As shown in Figure 7, the photoinduced current density of the g-C₃N₄ thin-film photoelectrode is approximately $-2 \mu\text{A}\cdot\text{cm}^{-2}$ under visible light illumination. However, the photo-induced current density of the Ag@AgCl/g-C₃N₄ thin-film photoelectrode is approximately $-560 \mu\text{A}\cdot\text{cm}^{-2}$ under visible light illumination, which is 280 times of that of g-C₃N₄. This result indicates that the photo quantum

yields of the Ag@AgCl/g-C₃N₄ composite are significantly improved, which could be based on the following two reasons: On one hand, more photoinduced electrons and holes are generated due to the strong light absorption and visible light responsive capability of Ag@AgCl based on the results shown in Figure 4; on the other hand, the interfacial electric field formed on the interface between g-C₃N₄ and Ag@AgCl increases the separation efficiency of the photogenerated electrons and holes, and hence increases the photoinduced current. These two reasons mentioned above result in the significant promotion of the photocatalytic degradation performance of the Ag@AgCl/g-C₃N₄ composite. As the results shown in Figure 7, the photoinduced current of both g-C₃N₄ and Ag@AgCl/g-C₃N₄ photoelectrodes are cathodic current, reflecting the characteristics of a p-type semiconductor. This result indicates that the photogenerated electrons will participate in the reduction reactions occurred on the surface of the photoelectrode, while, the photogenerated holes will capture the electrons from the counter electrode.

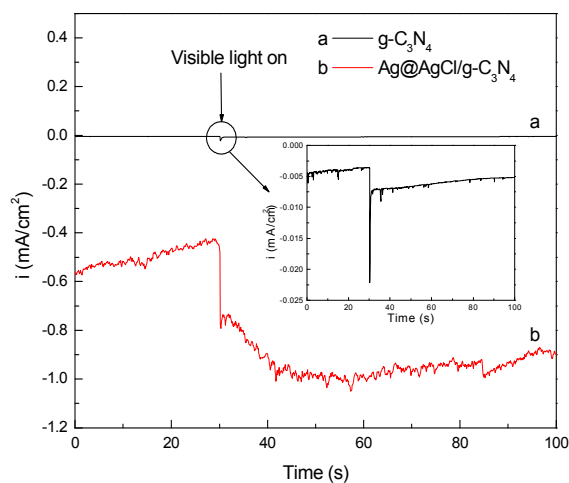


Figure 7. Photoinduced i-t curve of (a) g-C₃N₄ and (b) Ag@AgCl/g-C₃N₄ (0 V vs Ag/AgCl).

The Mott–Schottky method was employed to determine whether the heterojunction electric field was formed on the interface between g-C₃N₄ and Ag@AgCl. As we know, different semiconductor materials have different Fermi level potentials.⁵¹ When a composite is formed by two different semiconductor materials, a new balance of the Fermi level will eventually reach due to the opposite movement of the Fermi levels of these two semiconductors. With the shift of the Fermi level, electrons and holes will exchange on the interface between them and an interfacial electric field will be built. Meanwhile, the conduction band and the valence band will shift with the movement of the Fermi levels. Band bending will be formed on the interface and the flat band potential of the semiconductors will be subsequently changed. Therefore, the formation of the heterojunction electric field could be detected by measuring the changes of the flat band potential using the Mott–Schottky method. Figure 8 shows the Mott–Schottky plots of g-C₃N₄ and the Ag@AgCl/g-C₃N₄ composite thin-film photoelectrodes in 0.1 M Na₂SO₄ under dark condition. The flatband potential of a semiconductor material can be determined by extrapolating to $C^{-2} = 0$. The flatband potential of g-C₃N₄ was approximately -1.33 V (vs Ag/AgCl) (Figure 8), while, that of the Ag@AgCl/g-C₃N₄ composite positively shifts to 0.067 V. The difference in their flatband potential demonstrates that a heterojunction electric field was formed on the

interface between g-C₃N₄ and Ag@AgCl. And, the existence of this electric field significantly increases the separation efficiency of the photogenerated electrons and holes and therefore dramatically enhances the photocatalytic degradation performance of the Ag@AgCl/g-C₃N₄ composite.

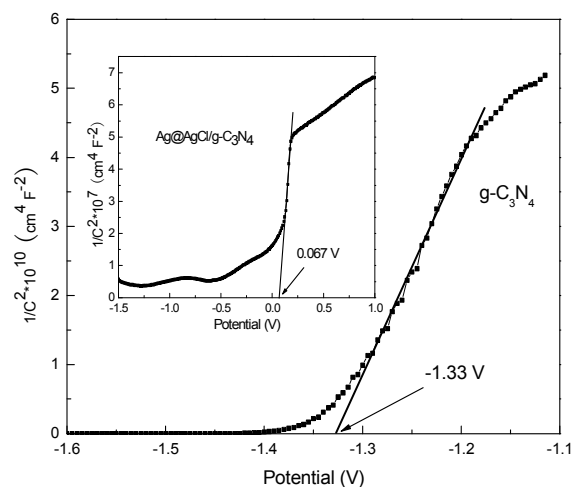


Figure 8. Mott-Schottky plots of g-C₃N₄ and Ag@AgCl/g-C₃N₄ composite photoelectrodes in 0.1 M Na₂SO₄ solution under dark.

According to the Mott-Schottky plots shown in Figure 8, both g-C₃N₄ and the Ag@AgCl/g-C₃N₄ composite exhibit the characteristics of an n-type semiconductor. This result is different from that shown in Figure 7, in which a cathodic photoinduced current is observed. It is well known that the Fermi level of a semiconductor will change with the applied bias potential. If an n-type semiconductor is loaded on a conductive substrate, the semiconductor would gather positive charges and the conductive substrate would gather negative charges when the applied bias potential increases from negative direction. At this

time, the Fermi level of this semiconductor will positively shift and move close to the valence band of the semiconductor, and the semiconductor type was converted from n type into p type. In Figure 7, with the bias potential of 0 V (vs Ag/AgCl), the Fermi levels of g-C₃N₄ and Ag@AgCl/g-C₃N₄ were positive shifted and the characteristics of them exhibited as p-types.

Figure S2 shows the photoluminescence spectroscopy of g-C₃N₄ and Ag@AgCl/g-C₃N₄. For g-C₃N₄, a strong, luminous broad peak emerged from 400 nm to 650 nm. However, for Ag@AgCl/g-C₃N₄, this light-emitting broad peak was absent, indicating that the presence of Ag@AgCl can effectively inhibit the annihilation of the photogenerated electrons and holes and effectively improve their separation efficiency and increase the lifetime of the photogenerated electrons, thereby enhance the RhB photocatalytic degradation efficiency and photoelectrochemical properties of the Ag@AgCl/g-C₃N₄ composite.

The scavengers of the photogenerated holes and electrons were added into the RhB dye solution to further study the promotion mechanism of the photocatalytic degradation performance of the Ag@AgCl/g-C₃N₄ composite. Figure S3 shows the photocatalytic RhB degradation curves of Ag@AgCl/g-C₃N₄ composite in the RhB solution containing with the scavenger of the photogenerated holes (EDTA-2Na) or the photogenerated electrons (tert-butanol, BuOH).⁵¹ As shown in Figure S3, adding of 2 mM BuOH into the RhB dye does not significantly affect the photocatalytic RhB degradation rate

of the Ag@AgCl/g-C₃N₄ composite. As we know, BuOH can capture the photogenerated electrons, leading to the swift consumption of the photogenerated electrons produced by the Ag@AgCl/g-C₃N₄ composite, therefore the photogenerated electrons by the Ag@AgCl/g-C₃N₄ composite cannot contribute to the photocatalytic RhB degradation in the BuOH-containing RhB solution based on the results shown in Figure S3. However, the photocatalytic degradation performance of the Ag@AgCl/g-C₃N₄ composite significantly decreased by adding 2 mM EDTA-2Na in the RhB solution as compared with that in the RhB solution in the absence of EDTA-2Na (Figure 5) under visible light, revealing that the high photocatalytic degradation performance of the Ag@AgCl/g-C₃N₄ composite mainly comes from the strong oxidizing capability of the photogenerated holes.

Figure 9 schematically shows the proposed mechanism for the promotion of the photocatalytic RhB degradation performance of the Ag@AgCl/g-C₃N₄ composite. When Ag@AgCl is loaded on the surface of g-C₃N₄, their Fermi levels will shift and finally get a balance which locates between the original Fermi levels of them. And, an efficient heterojunction electric field is established on the interface between Ag@AgCl and g-C₃N₄, which significantly improves the separation efficiency of the photogenerated electron-hole pairs. The photogenerated electrons by g-C₃N₄ can transfer to the conduction band of AgCl under the interfacial electric field and finally transfer to Ag nanoparticles. Ag can lower down the energy barriers of reduction reactions and it can be used as the catalytic center for such

reactions when the photogenerated electrons are transferred to Ag.⁵⁰ Meanwhile, the Ag nanoparticles on the surface of AgCl can absorb photons due to the SPR effect and generate separated electrons and holes. The electrons can participate in further dye reduction reactions. While, the holes can transfer to the valence band of AgCl and finally transfer to that of g-C₃N₄. The holes can then participate in the oxidation reactions there.

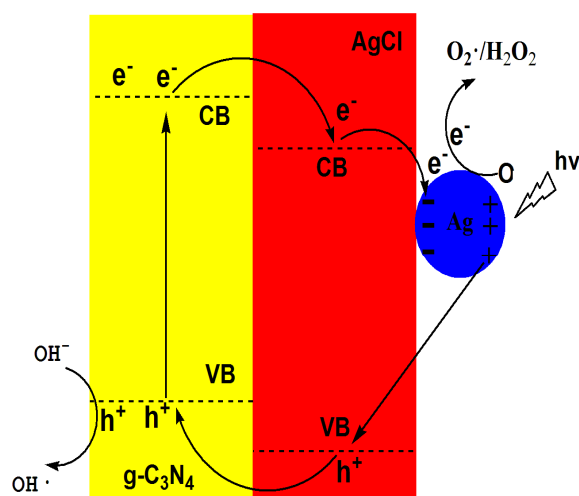


Figure 9. Schematic illustration of the significant promotion principles of the photocatalytic performance of the Ag@AgCl/g-C₃N₄ composite.

Through the processes mentioned above, the photogenerated electrons and holes can be effectively separated and transferred to different materials, leading to an effective inhibition of the recombination of them. Therefore, the photocatalytic degradation performance of g-C₃N₄ is dramatically increased after loading Ag@AgCl on the surface of g-C₃N₄.

Experimental

1 Preparation of g-C₃N₄ and the Ag@AgCl/g-C₃N₄ composite

g-C₃N₄ was prepared by directly heating dicyandiamine, which was placed in a semiclosed ceramic crucible with a cover, at 520 °C in a muffle furnace for 4 h at a heating rate of 10 °C·min⁻¹. The preparation of the Ag@AgCl/g-C₃N₄ composite was based on the method used by Wang et al.³⁸ 0.3 g of prepared g-C₃N₄ was dispersed in 20 mL deionized water, and the resulting mixture was ultrasonically vibrated for 30 min. Subsequently, silver nitrate ammonia (SNA) solution, which was prepared by dissolving 0.4 g of AgNO₃ into 2.3 mL NH₄OH solution (25 wt% NH₃), was then slowly added drop by drop into the dispersed liquid mixture of g-C₃N₄ and stirred for 10 min. After that, HCl solution, prepared by diluting 1.5 mL concentrated hydrochloric acid to 30 mL deionized water, was slowly added drop by drop into the liquid mixture of g-C₃N₄ and SNA solution under stirring. After 24 h of stirring at room temperature, 10 mL of methanol was added into the liquid mixture and subsequently this liquid mixture was transferred into a beaker with the temperature controlled at 25 °C by a water cooling system and irradiated for 30 min using a 300 W Xenon lamp under vigorous stirring. Some of the AgCl formed on the surface of g-C₃N₄ will be reduced to elemental Ag under light illumination. The Ag@AgCl/g-C₃N₄ composite was obtained by suction filtration and was then rinsed with deionized water and ethanol, and the Ag@AgCl/g-C₃N₄ powder was obtained after 6 h of vacuum drying at 60 °C.

In this work, the AgCl/g-C₃N₄ and Ag/g-C₃N₄ composites were used for comparative study on photocatalytic degradation performance of the Ag@AgCl/g-C₃N₄ composite. The AgCl/g-C₃N₄ composite was prepared following the same steps

mentioned above but removing the photo-reduction process, while, the Ag/g-C₃N₄ composite was prepared following the same steps mentioned above but removing the HCl solution adding steps.

2 Characterizations of the prepared composites

The morphologies and the microstructures of the synthetic composites were analyzed using a field emission scanning electron microscope (FESEM) (NoVaTM Nano SEM 430, FEI Company, USA) and a high-resolution transmission electron microscope (HRTEM, FEI Tecnai G20, FEI Company, USA). The crystalline structures and bonding information of the synthetic composites were analyzed using X-ray diffraction (XRD, D/MAX-2500/PC; Rigaku Co., Tokyo, Japan) and X-ray photoelectron spectroscopy (XPS, Axis Ultra, Kratos Analytical Ltd., England). The optical absorption properties were investigated using a UV/Vis diffuse reflectance spectrophotometer (U-41000; HITACHI, Tokyo, Japan). The photoluminescence intensity of the prepared samples was characterized using a fluorescence spectrometer (PL, Fluoro Max-4, HORIBA Jobin Yvon, France). The Brunauer–Emmett–Teller specific surface area was determined by a multipoint BET method (BET, 3Flex, Micromeritics, USA).

3 Photocatalytic degradation of Rhodamine B (RhB)

0.1 g prepared photocatalysts was added to 100 mL RhB with a concentration of 10 mg·L⁻¹ and stirred for 30 min in the dark. The light source was a 300 W Xenon lamp (PLS-SXE300, Beijing Changtuo Co. Ltd., Beijing, China). A 420-nm cutoff filter was used to remove light with wavelengths less than 420 nm and ultimately generate visible light (power energy density is 150 mW·cm⁻²). All of the photocatalytic degradation measurements were performed under visible light. The distance between the light source

and the dye liquid level is 10 cm. The temperature of the dye liquid was maintained at 25 °C using circulating water. The photocatalytic degradation stability of the Ag@AgCl/g-C₃N₄ composite was studied in this work. The concentration of RhB increased to 30 mg·L⁻¹. The photocatalyst was recycled by the centrifugation of the solution after dye degradation and the centrifugate was used for the next cycle of RhB degradation after sufficiently drying. Photocatalyst recycling tests were performed for six times in this work.

4 Photoelectrode preparation and photoelectrochemical measurements

An FTO glass (13 × 10 mm) was first ultrasonically cleaned with acetone of analytical grade for 5 min, rinsed with deionized water, and then dried with a clean, dry airflow. One longitudinal edge of the conductive side was then carefully covered with insulating tape, with the exposed effective area of the FTO glass measuring 1 cm². In total, 0.01 g of the prepared powder was mixed with 0.1 mL of deionized water in an agate mortar, and the mixture was carefully ground for 10 min to form a homogeneous suspension. Then, 0.025 mL of the as-prepared suspension was evenly distributed onto the exposed area of the conductive side of the FTO glass. The insulating tape on the edge of the FTO glass was removed after the suspension dried in the air. Finally, the FTO glass deposited with the as-prepared suspension was heated to 120 °C for 2 h under vacuum condition. A copper wire was connected to the conductive side of the FTO glass using conductive silver tape. The uncoated parts of the conductive side of the FTO glass were isolated with parafilm after the conductive silver tape had dried.

Photoelectrochemical measurements were performed in a three-electrode experimental system using CHI660D Electrochemical Workstation (Shanghai Chenhua Instrument Co., Ltd., Shanghai, China). The prepared photoelectrode, Ag/AgCl (saturated KCl) electrode, and Pt electrode acted as the working, reference, and counter electrodes, respectively. The potentials are reported on the Ag/AgCl (saturated KCl) scale. The photo, generated by a 300 W Xe arc lamp (PLS-SXE300, Beijing Changtuo Co. Ltd., Beijing, China), passed through a 420-nm cutoff filter, which was used to remove light with wavelengths less than 420 nm and ultimately generated visible light, and then a flat circular quartz window, equipped on the side of the three-electrode cell, and illuminated on the backside of the photoelectrode with an optical intensity of 150 mW·cm⁻². The variations of the photoinduced current density with time (i-t curve) were measured at a 0 V bias potential (vs AgCl) under visible light off and on. Mott-Schottky plots were measured in 0.1 M Na₂SO₄ solution at ambient temperature under dark condition. The potential range is -1.5 ~ 0.5 V and the frequency is 10 Hz with an AC voltage magnitude of 10 mV and a scan rate of 10 mV·s⁻¹.

Conclusions

In this work, the Ag@AgCl/g-C₃N₄ composite was prepared by in situ fabricating Ag@AgCl on the surface of g-C₃N₄ using deposition-precipitation and subsequently photo-assisted reduction. Both the photocatalytic degradation performance and the photocatalytic degradation stability of the Ag@AgCl/g-C₃N₄ composite are significantly improved compared with that of g-C₃N₄ and Ag@AgCl. The Ag@AgCl/g-C₃N₄ composite can

completely degrade RhB in 20 min under the illumination of visible light ($\lambda > 420$ nm). The results from UV/Vis diffuse reflectance spectroscopy show that the Ag@AgCl/g-C₃N₄ composite increases the light absorption intensity in visible light region due to the SPR effect, resulting in the significant increase of the yields of the photogenerated electrons and holes. The results from photoelectrochemical and electrochemical experiments show that an effective heterojunction electric field was formed on the interface between g-C₃N₄ and Ag@AgCl, which significantly strengthens the separation efficiency of the photogenerated electrons and holes, leading to a significant promotion of the photocatalytic degradation performance.

Acknowledgements

This work was financially supported by the National Natural Science Foundation of China (Grant No. 41376126) and the Hundreds-Talent Program of the Chinese Academy of Sciences (Y02616101L).

Notes and references

^a Key Laboratory of Marine Environmental Corrosion and Bio-fouling, Institute of Oceanology, Chinese Academy of Sciences, 7 Nanhai Road, Qingdao 266071, China.

^b School of Environment and Safety Engineering, Qingdao University of Science and Technology, 53 Zhengzhou Road, Qingdao 266042, China

Corresponding author, Prof. Zhuoyuan Chen; Email: zychen@qdio.ac.cn; Tel: +86-532-82898731; Fax: +86-532-82880498

- 1 J. D. Bass, C. D. Schaper, C. T. Rettner, N. Arellano, F. H. Alharbi, R. D. Miller, H.-C. Kim, *ACS Nano*, 2011, **5**, 4065.
- 2 X. Chen, L. Liu, P. Y. Yu, S. S. Mao, *Science*, 2011, **331**, 746.
- 3 K. Maeda, K. Teramura, D. L. Lu, T. Takata, N. Saito, Y. Inoue, K. Domen, *Nature*, 2006, **440**, 295.
- 4 Y. L. Lee, Y. S. Lo, *Adv. Funct. Mater.*, 2009, **19**, 604.

- 5 X. C. Wang, K. Maeda, A. Thomas, K. Takanabe, G. Xin, J. M. Carlsson, K. Domen, M. Antonietti, *Nat. Mater.*, 2009, **8**, 76.
- 6 S. Zhu, T. Xu, H. Fu, J. Zhao, Y. Zhu, *Environ. Sci. Technol.*, 2007, **41**, 6234.
- 7 F. Wang, C. Li, Y. Li, J. C. Yu, *App. Cata. B: Envir.*, 2012, **119-120**, 267.
- 8 K. Maeda, K. Domen, *Angew. Chem. Int. Ed.*, 2012, **51**, 9865.
- 9 J. Choi, H. Park, M. R. Hoffmann, *J. Phys. Chem. C*, 2010, **114**, 783.
- 10 G. Liu, Y. Zhao, C. Sun, F. Li, G. Q. Lu, H. M. Cheng, *Angew. Chem. Int. Ed.*, 2008, **47**, 4516.
- 11 K. G. Kanade, B. B. Kale, J. O. Baeg, S. M. Lee, C. W. Lee, S. J. Moon, H. Chang, *Mater. Chem. Phys.*, 2007, **102**, 98.
- 12 L. Etgar, P. Gao, Z. Xue, Q. Peng, A. K. Chandiran, B. Liu, M. K. Nazeeruddin, M. Gratzel, *J. Am. Chem. Soc.*, 2012, **134**, 17396.
- 13 W. Lee, S. K. Min, V. Dhas, S. B. Ogale, S. H. Han, *Electrochem. Comm.*, 2009, **11**, 103.
- 14 M. Wang, L. Sun, Z. Lin, J. Cai, K. Xie, C. Lin, *Energy Environ. Sci.*, 2013, **6**, 1211.
- 15 K. Li, B. Chai, T. Peng, J. Mao, L. Zan, *ACS Catal.* 2013, **3**, 170.
- 16 X. Xu, G. Liu, C. Random, J. T. S. Irvine, *Inter. J. Hydrogen Energy*, 2011, **36**, 13501.
- 17 F. Goettmann, A. Fischer, M. Antonietti, A. Thomas, *Angew. Chem. Int. Ed.*, 2006, **45**, 4467.
- 18 G. Li, D. Zhang, J. C. Yu, *Chem. Mater.*, 2008, **20**, 3983.
- 19 W. T. Sun, Y. Yu, H. Y. Pan, X. F. Gao, Q. Chen, L. M. Peng, *J. Am. Chem. Soc.*, 2008, **130**, 1124.
- 20 H. Wender, A. F. Feil, L. B. Diaz, C. S. Ribeiro, G. J. Machado, P. Migowski, D. E. Weibel, J. Dupont, S. R. Teixeira, *ACS Appl. Mater. Interfaces*, 2011, **3**, 1359.
- 21 S. Chuangchote, J. Jitputti, T. Sagawa, S. Yoshikawa, *ACS Appl. Mater. Interfaces*, 2009, **1**, 1140.
- 22 S. Emin, M. Fanetti, F. F. Abdi, D. Lisjak, M. Valant, V. D. R. Krol, B. Dam, *ACS Appl. Mater. Interfaces*, 2013, **5**, 1113.
- 23 S. C. Yan, Z. S. Li, Z. G. Zou, *Langmuir*, 2009, **25**, 10397.
- 24 J. S. Zhang, X. F. Chen, K. Takanabe, K. Maeda, K. Domen, Jan D. Epping, X. Fu, M. Antonietti, X. Wang, *Angew. Chem., Int., Ed.* 2010, **49**, 441.
- 25 Y. Wang, X. Wang, M. Antonietti, Y. Zhang, *ChemSusChem*, 2010, **3**, 435.
- 26 X. Zhang, X. Xie, H. Wang, J. Zhang, B. Pan, Y. Xie, *J. Am. Chem. Soc.*, 2013, **135**, 18.
- 27 Y. Zhang, A. Thomas, M. Antonietti, X. C. Wang, *J. Am. Chem. Soc.*, 2009, **131**, 50.
- 28 Y. Z. Zhang, T. Mori, J. H. Ye, M. Antonietti, *J. Am. Chem. Soc.*, 2010, **132**, 6294.
- 29 J. Zhang, J. Sun, K. Maeda, K. Domen, P. Liu, M. Antonietti, X. Fua, X. Wang, *Energy Environ. Sci.*, 2011, **4**, 675.
- 30 X. G. Ma, Y. L. Lv, J. Xu, Y. Liu, R. Zhang, Y. Zhu, *J. Phys. Chem. C*, 2012, **116**, 23485.
- 31 L. Ge, C. Han, J. Liu, Y. Li, *Applied Catalysis A: General*, 2011, **409-410**, 215.
- 32 Y. Di, X. Wang, A. Thomas, M. Antonietti, *ChemCatChem*, 2010, **2**, 834.
- 33 J. Dong, M. Wang, X. Li, L. Chen, Y. He, L. Sun, *ChemSusChem*, 2012, **5**, 2133.
- 34 S. C. Yan, S. B. Lv, Z. S. Li, Z. G. Zou, *Dalton Trans.*, 2010, **39**, 1488.
- 35 N. Yang, G. Q. Li, W. L. Wang, X. Yang, W. F. Zhang, *J. Phys. Chem. Solid*, 2011, **72**, 1319.
- 36 Y. J. Zhang, T. Mori, L. Niu, J. Ye, *Energy Environ. Sci.*, 2011, **4**, 4517.
- 37 Y. He, J. Cai, T. Li, Y. Wu, Y. Yi, M. Luo, L. Zhao, *Ind. Eng. Chem. Res.*, 2012, **51**, 14729.
- 38 P. Wang, B. Huang, X. Qin, X. Zhang, Y. Dai, J. Wei, M. H. Whangbo, *Angew. Chem., Int. Ed.*, 2008, **47**, 7931.
- 39 C. Hu, T. Peng, X. Hu, Y. Nie, X. Zhou, J. Qu, H. He, *J. Am. Chem. Soc.*, 2010, **132**, 857.
- 40 P. Wang, B. Huang, X. Zhang, X. Qin, Y. Dai, Z. Wang, J. Wei, J. Zhan, S. Wang, J. Wang, M. H. Whangbo, *Chem.-Eur. J.*, 2009, **15**, 1821.
- 41 C. An, S. Peng, Y. Sun, *Adv. Mater.*, 2010, **22**, 2570.
- 42 T. Morimoto, K. Suzuki, M. Torikoshi, T. Kawahara, H. Tada, *Chem. Commun.*, 2007, 4291.

- 43 Y. Xua, H.Xu, H. Li, J. Xia C. Liua, L. Liu, *Journal of Alloys and Compounds*, 2011, **509**, 3286.
- 44 P. Wang, B. B. Huang, X. Y. Qin, X. Y. Zhang, Y. Dai, M. H. Whangbo, *Inorg. Chem.*, 2009, **48**, 10697.
- 45 L. Zhang, K. H. Wong, Z. Chen, J. C. Yu, J. Zhao, C. Hu, C. Y. Chan, P. K. Wong, *App. Catal. A: General*, 2009, **363**, 221.
- 46 H. Zhang, X. Fan, X. Quan, S. Chen, H. Yu, *Environ. Sci. Technol.*, 2011, **45**, 5731.
- 47 Y. Xu, H. Xu, J. Yan, H. Li, L. Huang, J. Xia, S. Yin, H. Shu, *Coll. Surf.A: Physicochem. Eng. Asp.*, 2013, **436**, 474.
- 48 T. Zhou, Y. Xu, H. Xu, H. Wang, Z. Da, S. Huang, H. Ji, *Cera. Inter.*, 2014, **40**, 9293.
- 49 Q. Xiang, J. Yu, M. Jaroniec, *J. Phys. Chem. C*, 2011, **115**, 7355.
- 50 Y. Zheng, C. Chen, Y. Zhan, X. Lin, Q. Zheng, K. Wei, J. Zhu, *J. Phys. Chem. C*, 2008, **112**, 10773.
- 51 T. Xu, L. Zhang, H. Cheng, Y. Zhu, *Appl. Catal. B: Envir.*, 2011, **101**, 382.